OPEN ACCESS

Modeling Contact Resistance and Water Transport within a Cathode Liquid-Fed Proton Exchange Membrane Electrolyzer

To cite this article: Michael R. Gerhardt *et al* 2023 *J. Electrochem. Soc.* **170** 124516

Journal of The Electrochemical Society, 2023 **170** 124516

Modeling Contact Resistance and Water Transport within a Cathode Liquid-Fed Proton Exchange Membrane Electrolyzer

Michael R. Gerhardt,[1,z] Jenny S. Østenstad,[2,z] Alejandro O. Barnett,[2,z] and Magnus S. Thomassen[2,z]

[1]*SINTEF Industri, Batteries and Hydrogen Technologies, 7034 Trondheim, Norway*
[2]*Hystar AS, 1363 Høvik, Norway*

Conventional proton-exchange membrane (PEM) water electrolyzers use thicker membranes (>175 μm) than their PEM fuel cell counterparts (<25 μm), which reduces hydrogen crossover but also reduces electrolyzer efficiency due to the increased resistance. Reduction of hydrogen crossover is critical in conventional systems to avoid buildup of hydrogen in the anode above the lower flammability limit. New concepts for operating PEM water electrolyzers are emerging, such as the patented concept involving liquid water supply at the cathode while operating the anode with air, which reduces the safety concern related to hydrogen crossover using thin membranes. Experimental work has demonstrated the viability of this approach, but open questions remain regarding the interplay between water transport, water consumption, and cell performance, as well as identifying the components and material properties that enable high performance. In this work, a physics-based computational model of a cathode-fed PEM water electrolyzer was developed. The model highlights the importance of limiting contact resistance and explores the effect of cell compression on non-uniformity of current distributions. Sensitivity studies found that membranes up to 50 μm thick can be used without significant water transport limitations.

 [DOI: 10.1149/1945-7111/ad129d]

Manuscript submitted July 2, 2023; revised manuscript received November 27, 2023. Published December 20, 2023.

List of Symbols

Abbreviations

BPP	Bipolar plate
CL	Catalyst layer
GDL	Gas diffusion layer
HER	Hydrogen evolution reaction
ICR	Interfacial contact resistance
OER	Oxygen evolution reaction
PEM	Proton-exchange membrane
PTL	Porous transport layer
RH	Relative humidity

Greek

α	Water transport coefficient in the membrane
$\alpha_{i,j}$	Charge transfer coefficient for reaction i in direction j (anodic or cathodic)
β	Normalized cross-membrane water flux
ϵ	Porosity
ϵ_k	Volume fraction of phase k
η_i	Overpotential for reaction i, V
η_L, η_G	Viscosity of the liquid or gas phase, Pa s
γ_i	Surface tension of species i
κ	Ionic conductivity, S m^{-1}
λ	Number of water molecules absorbed per charged group
μ_i	Chemical potential of species i, J mol^{-1}
ω	Mass fraction
ϕ_i	Electric or ionic potential of phase i, V
ρ_i	Density of species or phase i, kg m^{-3}
σ	Electronic conductivity, S m^{-1}
θ	Contact angle
ξ	Electroosmotic drag coefficient

Roman

A	Area, m^2
a	Specific surface area, m^2 m^{-3}
C	Compressive strain
D_{ik}	Binary diffusion coefficient between species i and k, mol m^{-2} s^{-1}
E^0	Standard reduction potential, V
F	Faraday's constant, 96485 Cmol^{-1}
i	Current density, A m^{-2}
i_0	Exchange current density, A m^{-2}
i_{rxn}	Volumetric reaction rate, A m^{-3}
K	Permeability, m^2
k_{kl}	Rate constant for water phase change from phase k to phase l
M_i	Molar mass of species i, (kg/mol)
N_i	Molar flux of species i, mol m^{-2} s^{-1}
p	Pressure, Pa
R	Gas law constant, 8.314 J mol^{-1}K^{-1}
r_{con}	Area-specific contact resistance, Ω m^2
r_c	Critical radius, m
R_i	Rate of process or reaction i
s	Liquid saturation
S_i	Source term related to species or phase i
T	Temperature, K
$\vec{v}_k$	Velocity of phase k, m s^{-1}
W	Width, m
x_i	Mole fraction of species i

Subscripts

C	Capillary
Ch	Channel
eff	Effective
G	Gas
L	Liquid
La	Land
LV	Liquid-to-vapor transition (evaporation)
M	Membrane or ionomer phase
ML	Membrane-to-liquid transition
MV	Membrane-to-vapor transition
ref	Reference
S	Solid phase
sat	Saturation
T	Transition
u	Uncompressed

[z]E-mail: gerhardt.mike@gmail.com; jenny.ostenstad@hystar.com; alejandro.barnett@hystar.com; magnus.thomassen@hystar.com

Low-temperature water electrolysis is emerging as a viable method of carbon-emissions-free production of hydrogen gas.[1] In conventional proton-exchange membrane (PEM) water electrolysis, liquid water is fed to the anode side of the cell, where it is oxidized to protons and oxygen gas. These protons move across the PEM and are reduced at the cathode to hydrogen gas. Anode-fed PEM electrolyzers using renewable energy sources are capable of producing high-purity hydrogen with no greenhouse gas emissions. These traditional PEM electrolyzers, however, often use thick membranes to limit hydrogen crossover, which reduces the electrical efficiency by increasing cell resistance.

Feeding liquid water on the *cathode* side of the cell and air on the anode side simplifies mass transport on the anode to a single-phase oxygen enriched air stream and alleviates the concern of accumulation of hydrogen and oxygen gas. If hydrogen crossover is suspected, air flow can be increased to dilute the hydrogen and reduce the risk of flammable or explosive gas mixtures, thereby enabling use of thinner membranes with lower Ohmic resistance.[2] This design choice, however, requires adequate water transport from the cathode, across the PEM, to the anode, to ensure enough water is available at the anode to react.

Physics-based computational modeling has been previously used to study water transport problems in polymer-electrolyte fuel cells and electrolyzers.[3] Such models can provide spatially-resolved estimates of water content within the membrane and calculate the impact of water content differences on the conductivity and gas permeability of the membrane. In the context of electrolyzers, such models can also identify mass transport limitations related to water supply and availability.[4] Modeling of mass transport phenomena in PEM water electrolysis was recently reviewed.[5] No apparent consensus was found regarding dominant mechanisms of water and gas transport in the electrolyzer; differences between the models included whether phenomena such as coupled proton-water transport and two-phase flow are considered.

In addition to possible water transport issues, good electrical contact between the catalyst layer and the porous transport layer has been identified as a critical issue for PEM electrolyzers.[6] X-ray computed tomography studies have shown that the catalyst layers themselves may have poor in-plane conductivity due to the lack of a percolating network. Good electrical contact between the catalyst layer (CL) and the more conductive porous transport layer (PTL) can alleviate this issue and improve performance, making the electrical conductivity of the PTLs under electrolysis conditions important to understand.[7]

Modeling work on traditional PEM electrolyzers has demonstrated significant nonuniformities in current distribution and heat transport due to land-channel geometry.[8,9] The ridged land-channel architecture of electrolyzer flow fields, when pressed up against particularly soft carbon gas diffusion layers (GDLs), can cause significant deformation of the GDL, usually crushing the GDL under the lands while leaving it relatively intact over the channels.[10] The permeability, contact resistance, in-plane conductivity, and through-plane conductivity of carbon-fiber GDLs vary significantly when under compression,[11,12] which influences electrolyzer performance. Pore-network models have shown enhancements in through-plane transport of gases and liquids in porous media under compression alongside reductions in in-plane transport, because compression appears to reduce in-plane pore volume but not through-plane pore volume.[13]

Most of the models mentioned above are cell- or stack-level transport models, but other modeling methodologies exist to study electrolyzers at various scales. For example, the kinetics of the electrochemical reactions can be modeled through density functional theory, kinetic Monte-Carlo, and mean field microkinetic models, among other approaches. These methods and their application in multiscale electrochemical system modeling were highlighted in a recent review.[14] Empirical or analytical polarization-curve models can provide insight into dominant voltage loss mechanisms in electrolyzers without the complexity of a multiphysics, multidimensional transport model, and have also been recently reviewed.[15,16]

In this work, a computational model of a cathode-fed PEM electrolyzer is developed to address issues related to contact resistances under compression, water transport, and hydrogen crossover. First, we use the model to analyze experimental results using various materials as the PTL on the cathode side, demonstrating the important role of reducing electrical contact resistances between the PTL and CL on each side of the cell. Second, we report the results of a parameter variation study focused on identifying bottlenecks for water transport from the cathode to the anode, finding that thin membranes are critical for cathode-fed electrolysis.

Model Description

A two-dimensional model of a PEM electrolyzer was implemented in COMSOL Multiphysics® version 6.0. The model consists of domains for the bipolar plates, porous transport layers, and catalyst layers for both the anode and the cathode, as well as a membrane domain. The model physics include coupled proton and water transport within the membrane and ionomer, Butler-Volmer kinetics for the hydrogen evolution reaction, Tafel kinetics for the oxygen evolution reaction, two-phase flow models in the catalyst layers and porous transport layers, and Maxwell-Stefan multicomponent diffusion in the gas phase. This model is based on a prior vapor-phase PEM electrolyzer model published by Fornaciari et al.[4] Additionally, we add a simple compression model to adjust the properties of the PTL and CL based on local compression from the lands and a compression-dependent contact resistance. The governing Eqs. are listed in Eqs. 1 through 6 below:

$$\nabla\cdot\left(-\frac{\kappa_{\text{eff}}}{F}\nabla\phi_{\text{M}}-\frac{\xi\kappa_{\text{eff}}}{F^2}\nabla\mu_{\text{H}_2\text{O,M}}\right)=S_{\text{H}^+}, \quad [1]$$

$$\nabla\cdot\left(-\frac{\xi\kappa_{\text{eff}}}{F}\nabla\phi_{\text{M}}-\left(\frac{\xi^2\kappa_{\text{eff}}}{F^2}+\alpha_{\text{eff}}\right)\nabla\mu_{\text{H}_2\text{O,M}}\right)=S_{\text{H}_2\text{O,M}}, \quad [2]$$

$$\nabla\cdot\left(-\rho_{\text{L}}\frac{K_{\text{L}}}{\eta_{\text{L}}}\nabla p_{\text{L}}\right)=S_{\text{L}}, \quad [3]$$

$$\nabla\cdot\left(-\rho_{\text{G}}\frac{K_{\text{G}}}{\eta_{\text{G}}}\nabla p_{\text{G}}\right)=S_{\text{G}}, \quad [4]$$

$$\nabla\cdot\left(-\rho_{\text{G}}\omega_i\sum_k\bar{D}_{ik}\left(\nabla x_k+(x_k-\omega_k)\frac{\nabla p_{\text{G}}}{p_{\text{G}}}\right)+\rho_{\text{G}}v_{\text{G}}\omega_i\right)=S_{i,G}, \quad [5]$$

$$\nabla\cdot(-\sigma\nabla\phi_{\text{S}})=i_{\text{rxn}}. \quad [6]$$

These Equations represent conservation of protons (1) and water (2) in the membrane, conservation of mass in the liquid (3) and gas (4) phases in the porous medium, diffusion of each individual gaseous species (5), and conservation of current in the electronically conducting phases (6). The specific definitions of each term are discussed in the Sections below.

Transport of water and protons in the membrane and ionomer.—The approach of Weber and Newman[17] is used to model coupled water and proton transport through the proton-exchange membrane and the ionomer phase in each catalyst layer. In this model, the proton flux and water flux are coupled, and both fluxes depend on both the electric potential in the membrane, ϕ_{M}, and the chemical potential of water in the membrane, $\mu_{\text{H}_2\text{O,M}}$, as shown in Eqs. 1 and 2. The membrane is assumed to have different transport

properties when exposed to liquid water instead of water vapor. In particular, the water transport coefficient α_{eff} is defined to enable a smooth transition between diffusion down a chemical potential gradient in the vapor-equilibrated case and pressure-driven Darcy flow in the liquid-equilibrated case. The water transport coefficient α_{eff}, ionic conductivity κ_{eff}, and electroosmotic drag coefficient ξ are defined in Figure A·1 and Table A·I in the Appendix, and F is Faraday's constant.

The conductivity and water transport coefficients depend on the water content λ, which is defined as the ratio of water molecules to negatively-charged groups in the PEM (typically sulfonates). The water content is calculated from the water activity, which in turn is calculated from the chemical potential of water as described in Table A·II and Table A·III.

Protons in the membrane are generated by the oxygen evolution reaction (OER) at the anode and consumed by the hydrogen evolution reaction (HER) at the cathode. The rate of proton generation and consumption is controlled by the electrochemical reaction rate i_{rxn}:

$$S_{H^+} = \frac{i_{\text{rxn}}}{F}, \quad [7]$$

where a positive i_{rxn} signifies oxidation.

In this work, as in the original model on which this work is based,[4] the proton concentration is assumed equal to the concentration of negatively charged groups in the PEM. The use of deionized (DI) water in this work should mitigate any issues caused by cationic contaminants, which have been shown to increase cell voltage in PEM water electrolysis.[18] A recent review has also suggested that the local pH within a PEM electrolyzer may change after several hours of operation, contributing to corrosion of the bipolar plates.[19] Developing an understanding for the pH and how it changes within the electrolyzer, while beyond the scope of this work, would be a beneficial contribution to overall understanding and optimization of PEM electrolyzer performance and lifetime.

Water can enter or exit the membrane phase via phase changes to the liquid or vapor phase, and it is consumed by OER at the anode. These effects are modeled through adding source terms to the water conservation equation. At the anode,

$$S_{H_2O,M} = -R_{MV} - \frac{i_{\text{rxn}}}{2F}, \quad [8]$$

and at the cathode,

$$S_{H_2O,M} = -R_{MV} - R_{ML}, \quad [9]$$

where R_{MV} represents the rate of water phase change from the membrane phase to the vapor phase, and R_{ML} is the rate of water phase change from the membrane phase to the liquid phase. These are each calculated from the chemical potentials as defined in Table I.

Two-phase flow of water in the CL and PTL/GDL.—In the porous media, mass conservation equations are applied to the liquid (Eq. 3) and gas (Eq. 4) phases in the porous media, assuming Darcy's law applies individually to each phase as follows:

$$v_G = -\frac{K_G}{\eta_G}(\nabla p_G), \text{ and} \quad [10]$$

$$v_L = -\frac{K_L}{\eta_L}(\nabla p_L), \quad [11]$$

where v_i represents the volume-averaged velocity of phase i. Both liquid and gas phases are modeled on the cathode side of the cell, where liquid water and hydrogen gas flow through the GDL and CL, whereas the anode side is assumed single-phase gaseous flow. This work follows previous two-phase flow approaches such as Zenyuk et al.[20] The viscosities for the gas (η_G) and liquid (η_L) phases, as well as the densities ρ_G and ρ_L, are given in Table A·IV. The permeabilities for each phase, K_L and K_G, are defined as follows:

$$K_L = K_{\text{sat}} s^3, \text{ and} \quad [12]$$

$$K_G = K_{\text{sat}}(1 - s)^3, \quad [13]$$

where the saturated permeability K_{sat} of each component is listed in Table II, and s is the saturation, defined as the fraction of pore space filled with liquid water. The saturation is a function of the capillary pressure p_C:

$$p_C = p_L - p_G. \quad [14]$$

The exact relationship between capillary pressure and saturation relationship comes from porosimeter measurements and is implemented as a lookup table in the model. Mercury intrusion porosimetry of a titanium PTL is shown in Fig. A·2 and shows the cumulative volume of mercury introduced into the porous PTL as a function of the mercury pressure applied. This data was corrected for the wetting properties of water and converted to saturation as a function of capillary pressure as follows. We assumed that the maximum intrusion measured represented a mercury saturation of 1, and normalized the intrusion data accordingly to give mercury saturation as a function of applied mercury pressure. Mercury is non-wetting, with an observed contact angle on the Ti PTL of approximately 130°. Thus, mercury intrusion into a vacant PTL should be similar to air intrusion into a flooded PTL, because air is similarly non-wetting with a contact angle of approximately 133°. This contact angle was calculated from a measured PTL-water contact angle of 47°.[21] From the Young-Laplace equation, the applied mercury pressure defines a critical radius r_c, which represents the radius of the smallest mercury-filled pore in the case of mercury intrusion:

$$r_{c,Hg} = -\frac{2\gamma_{Hg}\cos(\theta_{Hg})}{p_{C,Hg}}, \quad [15]$$

where γ_{Hg} represents the mercury-air surface tension and θ_{Hg} represents the contact angle of mercury on the titanium PTL.

The capillary pressure at which air intruding into water will fill those same pores is calculated as:

Table I. Proportionality constants and definitions for the phase-change source terms.

Phase transition	Rate constant ($\text{mol}^2\ \text{m}^{-3}\ \text{s}^{-1}\ \text{J}^{-1}$)	Rate equation
Membrane-bound to vapor	$k_{MV} = 1$	$R_{MV} = k_{MV}(\mu_{H_2O,M} - \mu_{H_2O,V})$
Membrane to liquid	$k_{ML} = 500$	$R_{ML} = k_{ML}(\mu_{H_2O,M} - \mu_{H_2O,L})$
Liquid to vapor	$k_{LV} = 100$	$R_{LV} = k_{LV}(\mu_{H_2O,L} - \mu_{H_2O,V})$

Table II. Structural characteristics of the porous GDL, PTL, and CLs.

Component	K_{sat} (m^2)	ϵ_S	ϵ_M
Cathode GDL	1×10^{-12}	0.2	0
Cathode CL	1×10^{-12}	0.2	0.5
Anode PTL	9.97×10^{-11}	0.45	0
Anode CL	9.97×10^{-11}	0.45	0.5

$$p_{C,\ air-water} = -\frac{2\gamma_{air}\cos(\theta_{air})}{r_{c,Hg}} = \frac{\gamma_{air}\cos(\theta_{air})}{\gamma_{Hg}\cos(\theta_{Hg})}p_{C,Hg}. \quad [16]$$

The mercury porosimetry data in Fig. A·2 can be used to calculate the air saturation for a given capillary pressure by correcting the capillary pressure by the ratio shown above and finding the equivalent mercury saturation. The water saturation is then calculated by subtracting the air saturation from 1. The results of this correction procedure are also shown in Fig. A·2.

Gaseous species diffusion.—The transport of each individual gas species (water, oxygen, hydrogen, and nitrogen) by diffusion and convection is given by the Maxwell-Stefan equation for multicomponent diffusion (Eq. 5), in which ω_i and x_i represent the mass and molar fraction of component i, respectively, and v_G represents the velocity of the gas. The inverted binary diffusion coefficient matrix $\bar{D}_{ik}$ is automatically computed by COMSOL from the standard binary diffusion coefficients pD_{ik} given in Table A·V, after they are corrected for the gas pressure and volume fraction as follows:

$$D_{ik,eff} = \frac{pD_{ik}}{p_G}(\epsilon_G)^{1.5}, \quad [17]$$

where ϵ_G represents the volume fraction of the gas phase. For details of the calculation of the diffusion coefficient, see Refs 4, 22.

The source terms for each species in the gas phase are defined by region in Table III. Note that gas-phase water is not directly consumed by an electrochemical reaction, so i_{rxn} does not appear in the conservation equation for gas-phase water. Instead, membrane-bound water is consumed by the oxygen evolution reaction at the anode.

Electron transport and electrochemical reactions.—Each catalyst layer is modeled as a porous electrode consisting of an electron-conducting solid (catalyst particles), an ion-conducting solid (ionomer), and a gaseous mixture, with the cathode catalyst layer also containing liquid water. The solids are assumed homogeneously distributed. Electronic current flows down the potential gradient through the catalyst particles, PTL, GDL, and bipolar plate, as in Eq. 6, in which σ represents the electronic conductivity of the material. The electronic conductivity is assumed isotropic in all materials except the cathode CL and GDL, which have different in-plane and through-plane conductivities. The conductivity values are given in Table IV.

As shown in Eqs. 6 and 1, conservation of electronic and ionic current depends on the reaction rate i_{rxn}. At the anode, the rate of the oxygen evolution reaction is calculated by a Tafel expression:

$$i_{rxn,OER} = ai_{0,OER}a_{H_2O,M}\exp\left(\frac{\alpha_{OER,a}F}{RT}\eta_{OER}\right), \quad [18]$$

and at the cathode, the rate of the hydrogen evolution reaction is calculated by a Butler-Volmer expression:

$$i_{rxn,HER} = ai_{0,HER}\left(\frac{p_{H_2}}{p_{ref,H_2}}\exp\left(\frac{\alpha_{HER,a}F}{RT}\eta_{HER}\right) - a_{H_2O,M}\exp\left(-\frac{\alpha_{HER,c}F}{RT}\eta_{HER}\right)\right), \quad [19]$$

with the variables as defined in Table V.

Compression effects.—The channel wall (also called the rib or land) concentrates the clamping pressure applied across the cell, according to both simulations and experimental observations.[10,11] The degree of concentration depends on the mechanical properties of the GDL as well as the geometry of the flow field. Rather than incorporate a fully-coupled mechanics model with deforming geometry, which can increase the computational complexity, we instead use the following parameterized function to approximate the results shown in Kleemann et al.:[10]

$$p_{comp}(x) = p_{max} - (p_{max} - p_{min})\left(\tanh\left(\frac{\left(x + \frac{W_{Ch}}{2}\right)}{W_T}\right) - \tanh\left(\frac{\left(x - \frac{W_{Ch}}{2}\right)}{W_T}\right)\right), \quad [20]$$

in which the local compression pressure $p_{comp}(x)$ is assumed to transition from a high value p_{max} over the land to a low value p_{min} over the channel, with a transition region of width W_T centered at the channel edges. Typically, the average compression pressure p_{avg} is known, or can be estimated, based on the cell assembly procedure. Given these values, the maximum compression pressure p_{max} can be estimated as follows:

$$p_{max} = \frac{p_{avg}(W_{La} + W_{Ch}) - p_{min}W_{Ch}}{W_{La}}. \quad [21]$$

The values for each parameter mentioned above are listed in Table VI.

Contact resistance between components.—Pressure-dependent contact resistances were implemented at each bipolar plate (BPP)/PTL interface and each PTL/CL interface by adding a discontinuity

Table III. Definition of source terms for the gaseous species in the model, where M_i is the molar mass of species i. Definitions of the phase change terms R_{MV} and R_{LV} are given in Table I.

	aPTL	aCL	Membrane	cCL	cPTL
S_{H_2}	—	—	—	$M_{O_2}\frac{i_{rxn}}{2F}$	—
S_{O_2}	—	$M_{O_2}\frac{i_{rxn}}{4F}$	—	—	—
S_{N_2}	—	—	—	—	—
S_{H_2O}	—	$M_{H_2O}R_{MV}$	—	$M_{H_2O}(R_{LV} + R_{MV})$	$M_{H_2O}R_{LV}$

Table IV. Electronic conductivities for each component. The local compressive strain C_{local} is calculated using Fig. 2 and the local pressure from Eq. 20. σ_x represents in-plane and σ_y through-plane conductivities.

Component	σ (S cm^{-1})
Bipolar plate[a]	1.3 e4
Anode PTL and CL[b]	1.3 e4
Cathode PTL and CL[c], σ_x	$131C_{\text{local}}{}^3 - 79.9C_{\text{local}}{}^2 + 47.0C_{\text{local}} + 25.9$
Cathode PTL and CL[c], σ_y	$125C_{\text{local}}{}^3 - 166C_{\text{local}}{}^2 + 93.9C_{\text{local}} - 45.9$

a) From the COMSOL Material Library, Stainless Steel 455 Annealed. b) Conservative estimate considering a conductivity of over 2e6 S/m for bulk Ti. c) Cubic polynomial fit to data from Nitta et al.[11]

Table V. Properties relevant to the electrochemical reaction kinetics.

Symbol	Name	Definition	
a	Specific surface area	1×10^5 m^{-1}	
η_i	Overpotential	$\phi_S - \phi_L - E_i^0$	
		HER property	OER property
$\alpha_{i,a}$	Anodic charge transfer coefficient	1	2
$\alpha_{i,c}$	Cathodic charge transfer coefficient	1	—
E^0	Standard potential	0 V	1.23 V
i_0	Exchange current density	400 mA cm^{-2} [23,24]	1×10^{-7} mA cm^{-2}
p_{ref}	Reference pressure	1 atm	—

Table VI. Properties relevant to the compression effects submodel.

Symbol	Name	Definition
A_{cell}	Cell area	25 cm^2
A_{La}	Land area	7.584 cm^2
p_{avg}	Average compression pressure	50 N cm^{-2}
p_{max}	Maximum compression pressure	150 N cm^{-2}
p_{min}	Minimum compression pressure	0 N cm^{-2}
W_{Ch}	Channel width	2 mm
W_{La}	Land width	1 mm
W_{T}	Transition width	50 μm
ϵ_{u}	Uncompressed porosity	0.8

in the electric potential ϕ_S at each interface:

$$\Delta\phi_S = r_{\text{con}}(x) i_S \cdot \hat{n}, \qquad [22]$$

where $\Delta\phi_S$ represents the difference in ϕ_S across the interface, $\hat{n}$ is the vector normal to that interface, and $r_{\text{con}}(x)$ is the local area-specific contact resistance. Pressure-dependent contact resistance values were obtained from measurements and implemented in the model as a lookup table. The measurements are shown in Fig. 1 and report pressure and area-specific resistance relative to the cell's active area (25 cm^2). On the anode side, the Pt-PTL curve was used (blue circles in Fig. 1) for both the PTL/BPP and CL/PTL contact resistances. On the cathode side, the GDL-C2 contact resistance was used (orange circles in Fig. 1). To use these measurements as local properties in the model, they were scaled to the land-PTL contact area using the following relationships:

$$p_{\text{La}} = p_{\text{cell}} \left(\frac{A_{\text{cell}}}{A_{\text{La}}} \right), \text{ and} \qquad [23]$$

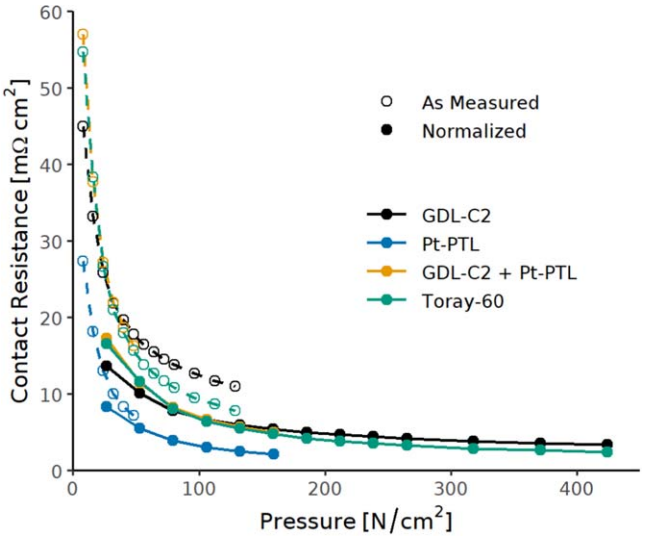

Figure 1. Measurement of contact resistance between the bipolar plate and various PTL and GDL materials.

$$r_{\text{con, La}} = r_{\text{con, cell}} \left(\frac{A_{\text{La}}}{A_{\text{cell}}} \right), \qquad [24]$$

in which the subscript *cell* indicates "relative to the cell active area", the subscript *La* indicates "relative to the land/PTL contact area", p represents compression pressure, r is the area-specific contact resistance, and A is the relevant area. Area values are given in Table VI. The "normalized" curves (filled circles in Fig. 1) have

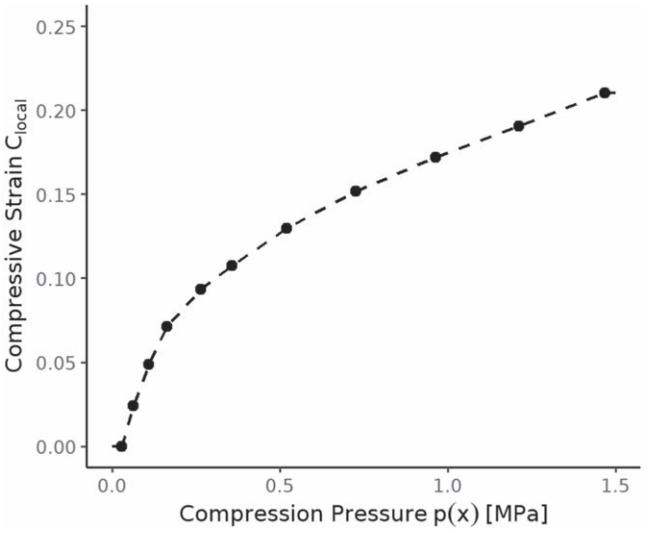

Figure 2. Compressive strain as a function of compressive pressure for the carbon GDL used in this work, based on measurements of Toray TGP-H-060.[10] Points indicate data extracted from Kleeman et al. and dashed lines indicate interpolation regions.

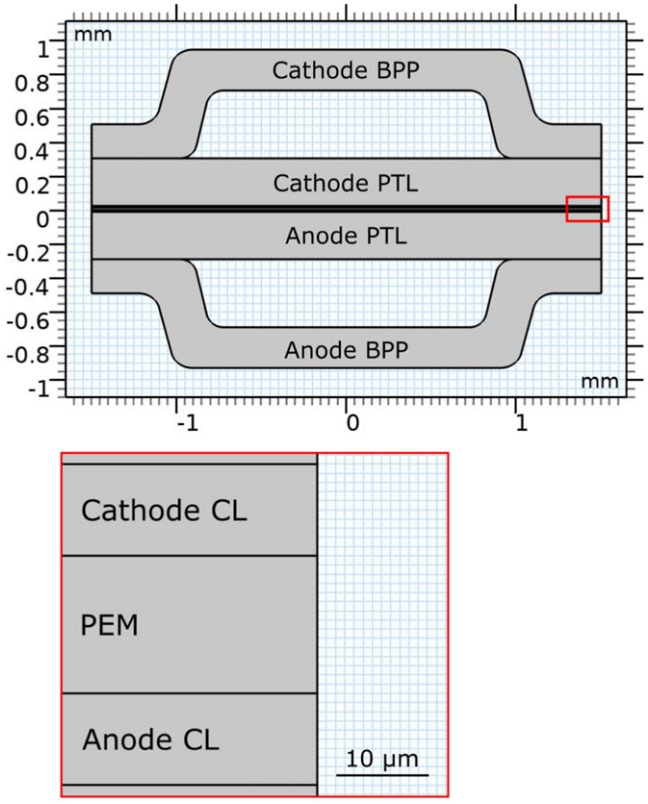

Figure 3. Schematic of the model computational domain, including a zoomed-in inset of the catalyst layers and proton-exchange membrane regions.

been scaled in this way from the original data to show $r_{\text{con,La}}$ as a function of p_{La}. This relationship is used to calculate the local contact resistance along each BPP/PTL interface and each PTL/CL interface as follows:

$$r_{\text{con}}(x) = b r_{\text{con,La}}(p_{\text{comp}}(x)). \quad [25]$$

The fitting parameter b takes a value of 0.625 at PTL/BPP interfaces to reproduce the measured HFR of 57 mΩ cm^2 for the Pt-PTL case and 2.3 at the PTL/CL interfaces to reproduce the measured HFR value of 90 mΩ cm^2 seen in the unsupported GDL experiments.

Effect of compression on material properties.—The model also estimates the effect of non-uniform compression on the porosity, permeability, and electronic conductivity of the porous carbon layers (the cathode GDL and CL). Using the assumed pressure distribution equation, a local compressive strain value was calculated based on experimental measurements of thickness under increasing compressive pressure given in Kleemann et al.[10] Specifically, the Toray TGP-H-060 thickness versus compressive pressure was normalized to the initial thickness to derive a compressive strain versus compressive pressure data set, which was implemented in COMSOL as a lookup table with linear interpolation as shown in Fig. 2.

The local porosity (that is, the volume fraction of space not filled with solid material) can be calculated from the uncompressed porosity $\epsilon_{\text{u}} = 1 - \epsilon_{\text{S}}$ and the local compressive strain C_{local}, by assuming that the compressive strain removes pore space:

$$\epsilon = 1 - \frac{1 - \epsilon_u}{1 - C_{\text{local}}}. \quad [26]$$

From the new local porosity, a local compressed permeability value is calculated by assuming the permeability varies with porosity according to the Kozeny-Carman relationship:[3]

$$K_{\text{comp}} = K_{\text{sat}}\left(\frac{(1-\epsilon_u)^2}{(1-\epsilon)^2}\right)\left(\frac{\epsilon^3}{{\epsilon_u}^3}\right). \quad [27]$$

Finally, the electrical conductivity for the cathode GDL and CL is adjusted based on the measured local compressive strain, using a cubic polynomial fit to data from Nitta et al.[11] The polynomial fits, as well as the electrical conductivities for the other components, are given in Table IV.

Model implementation.—The model was built in COMSOL Multiphysics® version 6.0. A to-scale schematic of the model is given in Fig. 3. The geometry was parameterized to enable studies of several configurations of parameter values and component thicknesses, with the base-case values given in Table VII.

A free triangular mesh was used in the bipolar plates, which allows COMSOL to automatically determine a mesh. Swept rectangular meshes were used in the PTLs, CLs, and membrane, with very fine resolution in the y-direction in the CLs and membrane as shown in the inset to Fig. 4.

Operational and boundary conditions.—For the electric potential, the outer (top) edge of the cathode BPP was grounded ($\phi_{\text{S}} = 0$), and at the outer edge of the anode BPP, a floating potential condition was used, in which ϕ_{S} was varied until the current density flowing through the boundary was equivalent to the desired cell current density normalized by the land width:

$$i_{\text{aBPP}} = i_{\text{cell}}\frac{W_{\text{Ch}} + W_{\text{La}}}{W_{\text{Ch}}}. \quad [28]$$

At each BPP/PTL and (PTL or GDL)/CL boundary, pressure-dependent contact resistances were applied by calculating a local value for the contact resistance from the calculated local compressive strain. This contact resistance, when applied, amounts to a potential difference across the boundary as described by Eq. 22. Insulating (no-flux) boundary conditions were used at the CL/membrane boundaries and all external-facing boundaries.

Table VII. Measurements of components in the model geometry.

Component property	Measurement
Bipolar plate thickness	200 μm
Bipolar plate channel wall angle	13.5°
Bipolar plate channel depth	400 μm
Bipolar plate fillet radius	100 μm
Cathode GDL thickness	280 μm
Cathode CL thickness	10 μm
Membrane thickness	15 μm
Anode PTL thickness	280 μm
Anode CL thickness	10 μm

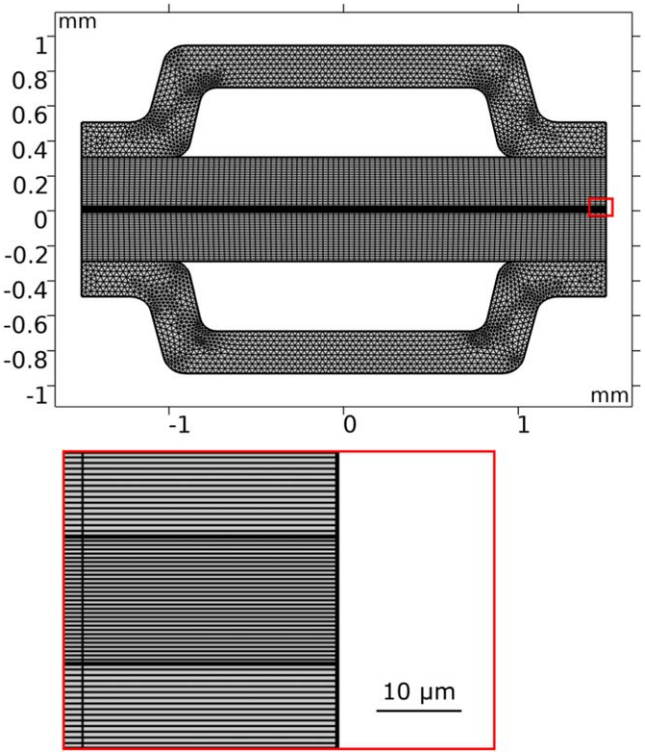

Figure 4. Mesh of the computaional domain, including a zoomed-in inset of the catalyst layers and proton-exchange membrane mesh.

For fluid flow, constant-pressure boundary conditions were specified at both channel boundaries. At the cathode, $p_L = p_G = 1$ atm at the channel/GDL boundary, and at the anode, where no liquid was simulated, $p_G = 1$ atm. At the PTL/BPP and GDL/BPP boundaries (the lands), as well as the CL/membrane boundaries and all other external boundaries, no-flux conditions were used.

For gaseous species transport, the gas composition was fixed at each channel boundary to be either air (21% O_2 and 79% N_2, dry) or hydrogen at the specified relative humidity, and no-flux conditions were used at the lands, x-facing boundaries, and the CL/membrane boundaries.

For membrane-bound water and protons, no-flux conditions were used at the CL/PTL and CL/GDL boundaries, as well as all x-facing CL and membrane boundaries. The temperature was assumed constant at 60 °C.

Experimental Methods

PTL characterization.—The interfacial contact resistance (ICR) measurements were performed using a technique adapted from Wang et al.[25] The titanium flow fields, and cathode diffusion media of interest (25 cm^2) were placed between two gold-coated copper plates. The pressure was varied between 0.2 and 2 MPa using a piston. A current of (2.00 ± 0.01) A was passed between the plates using a laboratory DC power supply (Xantrex XDL) while the voltage drop was monitored using a multimeter (Keithley 2000). The ICR is then calculated by dividing the resistance measured by the applied current density.

Mercury intrusion porosimetry was performed on a 0.5 g sample of the platinum-coated titanium PTL material (Pt-PTL) using an AutoPore IV 9500 (Micromeritics Instrument Corporation, Norcross, GA, USA).

Electrolyzer experiments.—Prototype catalyst coated membranes (CCMs) based on Gore SELECT®18 μm manufactured by IRD Fuel Cells were used to perform the model validation. The active area of the CCMs is 25 cm^2 using an iridium-based anode catalyst layer (CL) and Pt-based cathode CL, with loadings of 2 mg cm^{-2} Ir and 1 mg cm^{-2} Pt.

Titanium flow fields were used on both the anode and cathode side. Platinum-coated sintered titanium is used for the anode porous transport layers (Pt-PTL). The Pt protective coating over the Ti-based PTLs is usually employed in industrial PEM water electrolysis applications and applied to avoid titanium passivation that may result in high interfacial contact resistances. At the cathode, either Pt-PTL, Toray carbon paper 060 (Toray-60), Freudenberg GDL C2 (GDL-C2) or a combination of GDL-C2 and Pt-PTL was used. A clamping torque of 6 N m per bolt was used resulting in contact pressures of 0.2 to 0.5MPa on the active area.

After assembly, the PEM cells were subjected to a hydration and a break-in procedure. The hydration procedure included circulating 0.2 L min^{-1} of DI-water at both anode and cathode overnight at 40 °C. The break-in procedure involved changing the anode operating conditions from DI-water to 100% relative humidity (RH) humidified air according to Thomassen and Barnett.[2] The electrolyzer was polarized in increasing steps of 0.1 A cm^{-2} for 5 min until reaching 2 V, when the current was stepped back to 0 A cm^{-2} in the same increments. The polarization was repeated for temperatures 60 °C, 70 °C and 80 °C. The electrolyzer was then left at open circuit voltage overnight at 40 °C with recirculation of 0.2 L min^{-1} of DI-water at both anode and cathode. After the initial membrane hydration and break-in procedure, the cells were characterized by performing polarization curves under various operating conditions, i.e. temperature (60 °C to 80 °C range) and cathode side pressure (0 barg to 4 barg range). Polarization curve measurements were carried out following the testing procedure reported by Malkow et al.[26] Tests were performed under galvanostatic control with a cutoff voltage of 2 V or a current density upper limit of 4 A cm^{-2}. After each set of polarization curves, the cells were disconnected from the power supply and connected to a potentiostat (VMP3 with a 20 A Booster, BioLogic) with electrochemical impedance spectroscopy (EIS) capabilities. EIS was performed with a DC current of 18 A and an AC current of 2 A between 10 kHz and 0.1 Hz.

Results

Voltage increase when using compressible unsupported GDLs.—Polarization curves collected using four different PTL/GDL combinations on the cathode are shown in Fig. 5a. Three of the four polarization curves overlay each other, indicating that cell performance is not strongly affected by the choice of PTL/GDL combination at the cathode, with one exception. Using the soft, compressible Freudenberg GDL-C2 without any support on the cathode results in significantly higher voltage throughout the polarization curve, but placing a stiff Pt-coated Ti PTL between the GDL-C2 and the flow field results in similar performance to using only the Pt-PTL or using the stiffer Toray carbon paper GDL.

The difference in performance between lone GDL-C2 and the other three GDL/PTL combinations is driven by a difference in the measured high-frequency resistances of the four cells, reported in

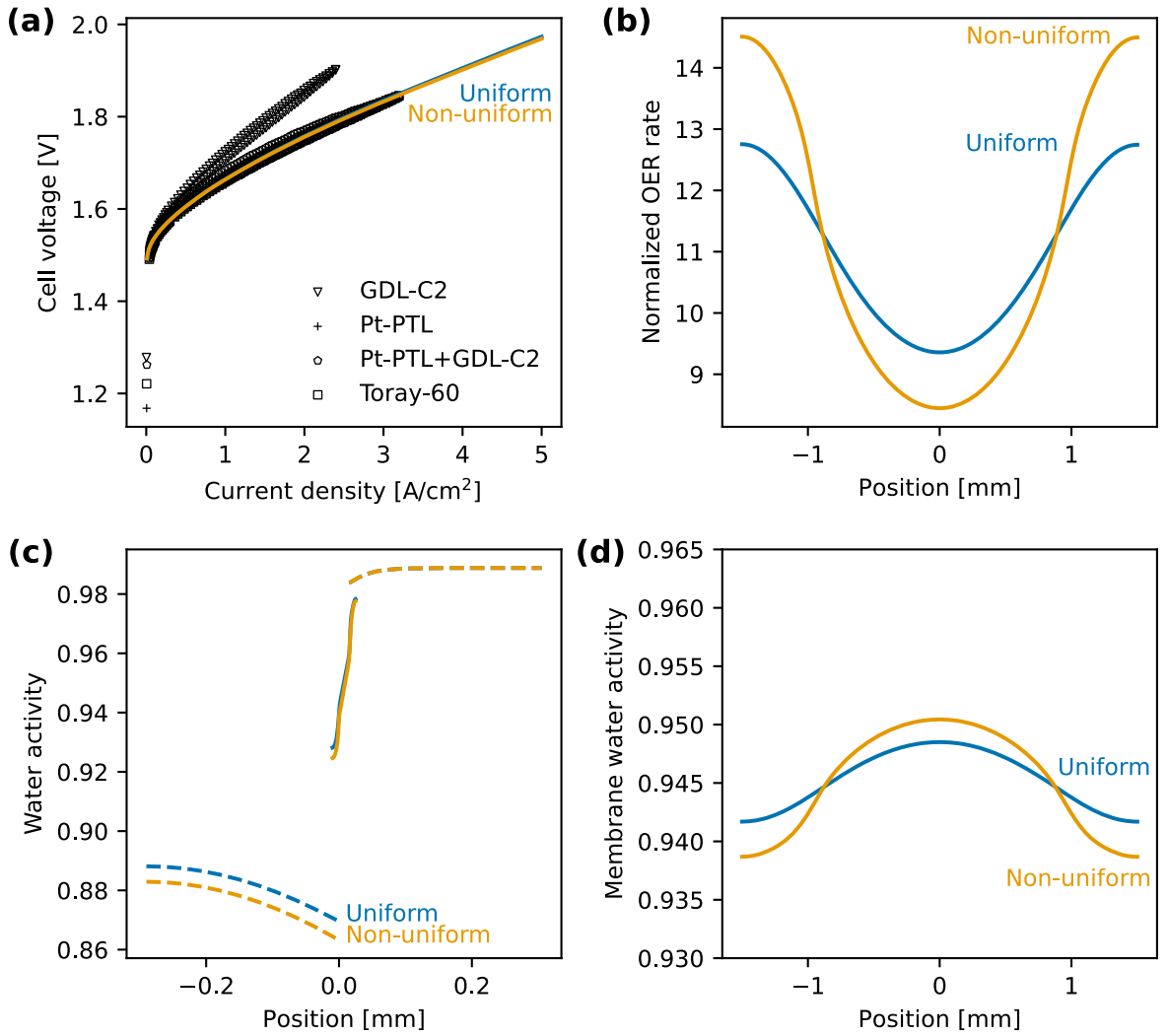

Figure 5. Modeled effect of non-uniform compression of the GDL material. **a.** Measured polarization curves at 60 °C for the four cathode PTL types described in the Experimental section (points), and calculated polarization curves assuming uniform or non-uniform compression (lines). **b.** Calculated OER reaction rate along the anode CL/membrane boundary, normalized by dividing the calculated rate by its expected value when uniformly distributed throughout the catalyst layer volume. **c.** Water activity through the cell cross-section above the center of the land. Dashed lines represent water activity in the vapor phase, and solid lines represent water activity in the membrane phase. The anode is on the left. **d.** Water activity along the membrane-aCL boundary, with lands on either side and the channel in the middle. The applied current is 4 A cm^{-2} in **b**, **c**, and **d**.

Table VIII. Measured high-frequency resistances for each of the PTL/GDL configurations studied in this work.

Cathode PTL/GDL configuration	Measured high-frequency resistance (mΩ cm^2)
GDL-C2	90
Pt-PTL	57
Pt-PTL + GDL-C2	57
Toray-60	63

Table VIII. The origin of the difference in the high-frequency resistance measurements is unclear. GDL-C2 alone does not exhibit a higher contact resistance on the bipolar plate in ex situ ICR measurements, (see Fig. 1), and if GDL-C2 had low electrical conductivity, the Pt-PTL + GDL-C2 cell would also exhibit greater high-frequency resistance than the Pt-PTL cell. Thus, we hypothesized that the land-channel structure of the bipolar plate applies non-uniform pressure, causing greater compression over the lands than over the channels when using soft GDL materials like GDL-C2, leading to reduced hydraulic permeability over the lands and reduced electrical conductivity over the channels. We tested this hypothesis by implementing these effects in the computational model as described in the "Compression Effects" Section above and found that such effects do not result in a large change in the polarization curve, as shown in Fig. 5a. Local properties such as the reaction distribution (Fig. 5b) and water activity (Fig. 5d) along the anode CL/membrane boundary become more non-uniform, however, which may affect cell operation or degradation over time and should be considered when designing an electrolysis cell.

The second hypothesis we considered was the existence of a compression-dependent contact resistance between the catalyst layers and the PTL or GDL on each side of the cell. To simulate this effect, we applied a local, pressure-dependent contact resistance scaled by a constant factor to match the measured high-frequency resistance of the GDL-C2 cell. Figure 6 shows the effect of including a contact resistance between the CL and PTL/GDL on each side of the cell and on both sides of the cell. In this case, including both contact resistances explains most of the voltage discrepancy between the two experiments, indicating that the performance limitations seen when using unsupported GDLs can be mostly attributed to a

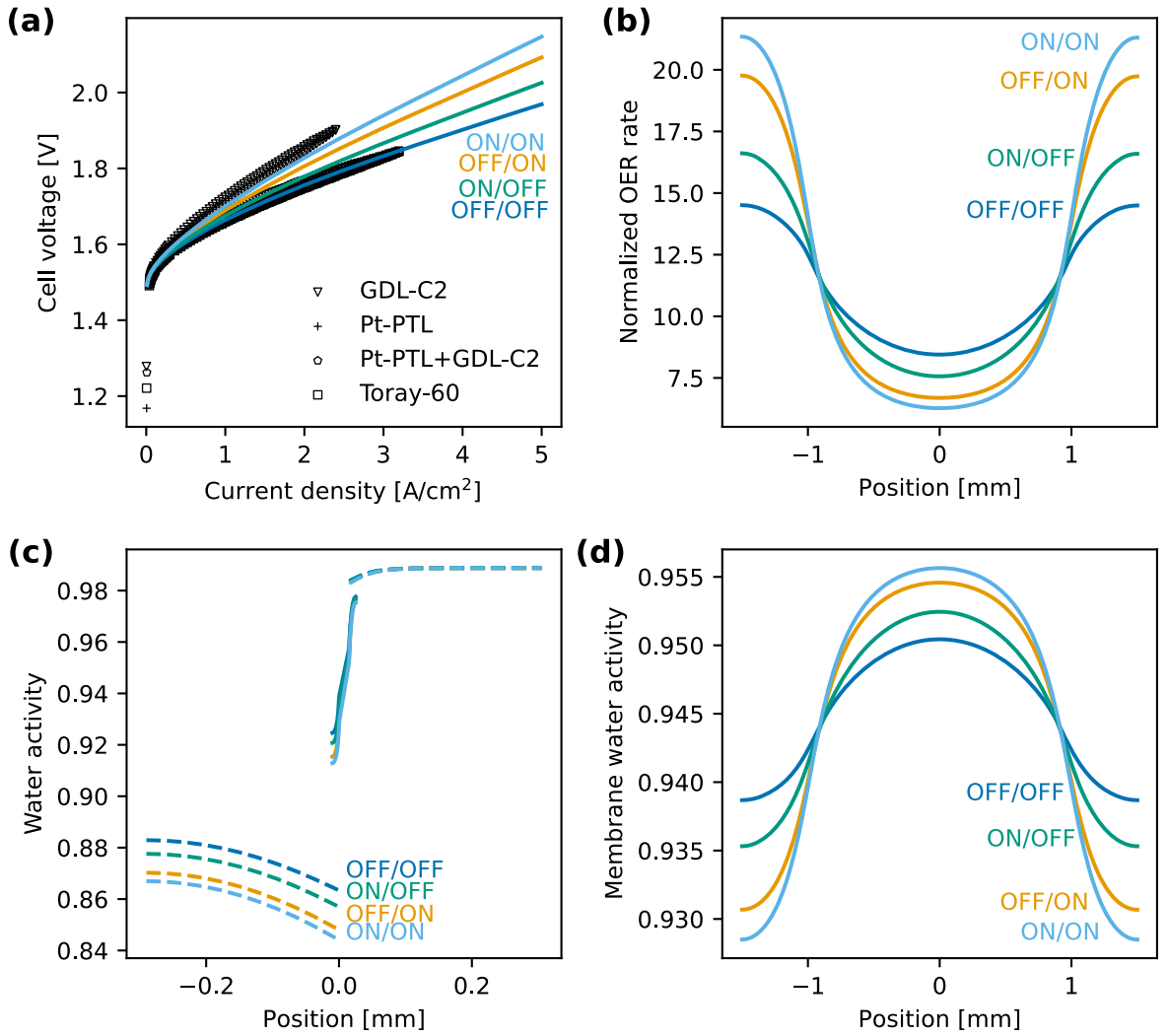

Figure 6. The effect of including a locally-varying compression-dependent contact resistance at the interface between the CL and the PTL or GDL. ON/OFF notation indicates whether contact resistances between the CL and the PTL or GDL are included on both electrodes (ON/ON), just the anode (ON/OFF), just the cathode (OFF/ON), or excluded from both (OFF/OFF). **a.** Measured polarization curves at 60 °C for the four cathode PTL types described in the Experimental section (points), and calculated polarization curves when including or excluding contact resistances at the anode CL/PTL interface and the cathode CL/GDL interface (lines). **b.** Calculated OER reaction rate along the anode CL/membrane boundary, normalized by dividing the calculated rate by its expected value when uniformly distributed throughout the catalyst layer volume. **c.** Water activity through the cell cross-section above the center of the land. Dashed lines represent water activity in the vapor phase, and solid lines represent water activity in the membrane phase. The anode is on the left. **d.** Water activity along the membrane-aCL boundary, with lands on either side and the channel in the middle. The applied current is 4 A cm^{-2} in **b**, **c**, and **d**.

change in contact resistance caused by the non-uniform compression of the GDL against the CL. One possible explanation for the difference between model and experiment is that, in addition to changes in contact resistance, the electrochemically accessible surface area could be changing with compression. For example, higher compressive forces under the land could improve connectivity between catalyst particles and increase accessible surface area.

The results in Fig. 6 also show that the water activity varies through the membrane (c) as well as along the membrane (d), which influences electrolyzer performance by affecting the availability of water for the OER and by changing the ionomer hydration. As a reactant in OER, water is consumed at the anode, and its presence or absence affects the equilibrium potential at the anode. As the OER reaction rate increases, so does water consumption, resulting in a decrease in water concentration and therefore water activity. The decrease in water activity in turn increases the equilibrium potential for OER, resulting in higher cell voltage. The water activity also has a strong impact on cell performance through influencing the ionomer hydration and thus its conductivity, as shown in Fig. A·1. Thus, for efficient electrolyzer operation it is imperative to keep the membrane well-hydrated to keep its conductivity high. Any successful cathode-fed liquid PEM electrolyzer must therefore maintain enough water flux from the cathode to the anode to prevent membrane dryout. The following Section addresses water flux concerns and demonstrates viable strategies for maintaining adequate membrane hydration.

Influence of water transport on cell performance.— *Varying anode relative humidity.*—The previous Section identified maintaining membrane hydration via cross-membrane water transport as critical for efficient operation of a cathode liquid-fed PEM electrolyzer. One immediate concern is the relative humidity (RH) of the air stream fed to the anode. With dry inlet air, the ionomer in the anode may begin to dry out and lose ionic conductivity. Our model shows, however, very little influence of air RH on polarization performance (Fig. 7). In all cases studied, the RH varied slightly along the CL/membrane boundary, but remained very high (>94%), indicating that the membrane retains water and remains hydrated due to the liquid water supply at the cathode. Figure 7b shows that despite the change in RH in the anode gas, the water activity in the membrane does not change, further demonstrating that water transport from the

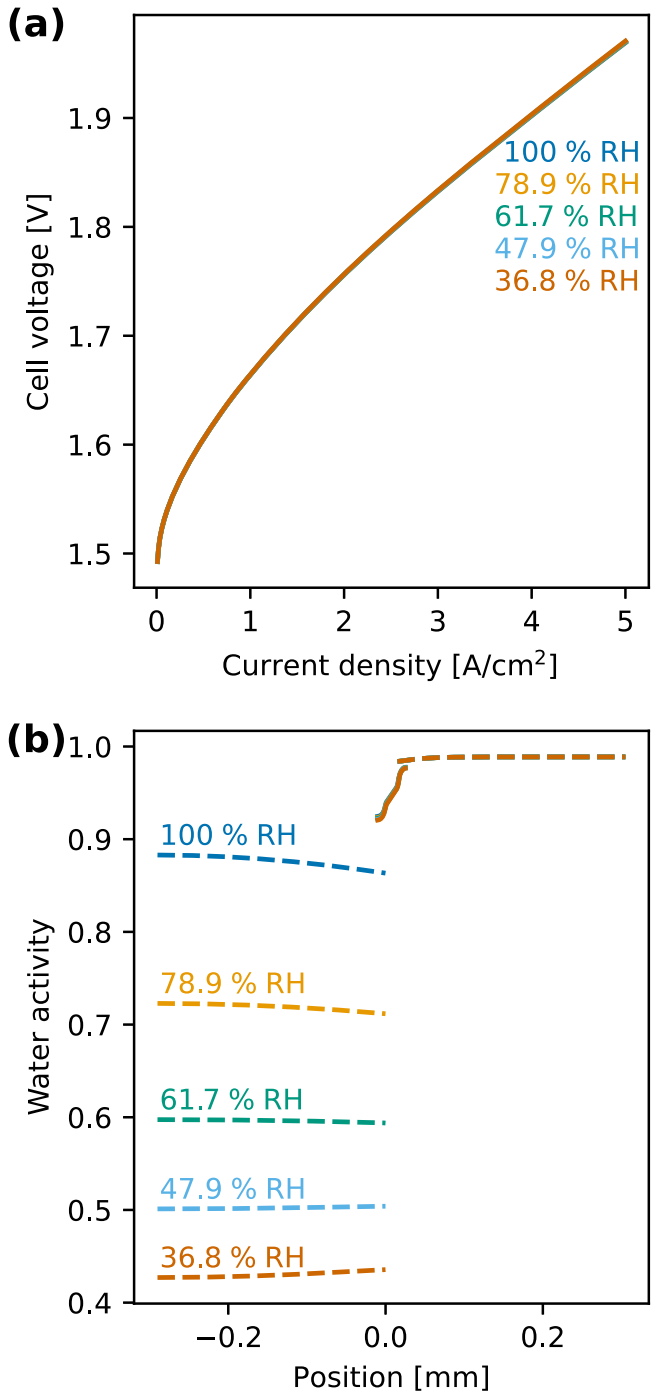

Figure 7. Simulated effect of varying the anode inlet relative humidity. **a.** Polarization curve, **b.** water activity through the cell cross-section over the land midpoint, with the anode on the left and the cathode on the right. Dashed lines in **b** represent water activity in the vapor phase. The applied current is 4 A cm^{-2} in **b**.

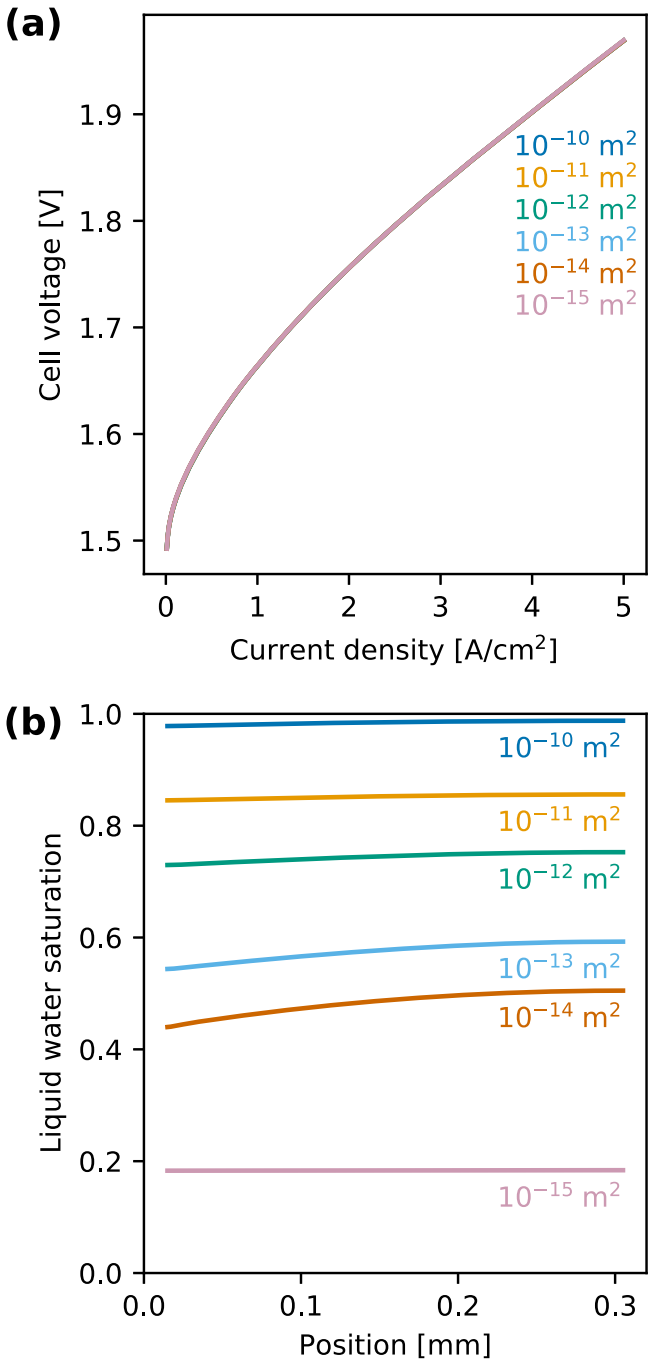

Figure 8. Simulated effect of varying the cathode GDL permeability. **a.** Polarization curve, **b.** average liquid saturation throughout the cathode catalyst layer at an applied current of 4 A cm^{-2}.

cathode through the membrane to the anode is adequate for electrolyzer operation.

Varying permeability of cathode GDL.—To study the importance of cathode liquid water transport, the cathode GDL permeability was varied, though no effect on cell voltage was found as shown in Fig. 8. Reaction distributions and water activities at the anode were also unaffected and are not shown for brevity. The liquid water saturation in the cathode catalyst layer did decrease substantially as the permeability was decreased, indicating potential liquid supply problems at even lower permeabilities. At a permeability of 10×10^{-16} m^2, the model failed to converge past about 2.5 A cm^{-2}, indicating a possible water supply limit, but no difference in polarization performance was observed before that point.

For very low permeability values, liquid water reaches its minimum saturation in the GDL in the cathode, as shown by Fig. 8b. Despite the change in water saturation, the model does not predict a change in membrane-bound water activity. Thus, the water content and hydration-dependent membrane properties remain the same, and no dryout is observed in the polarization curve.

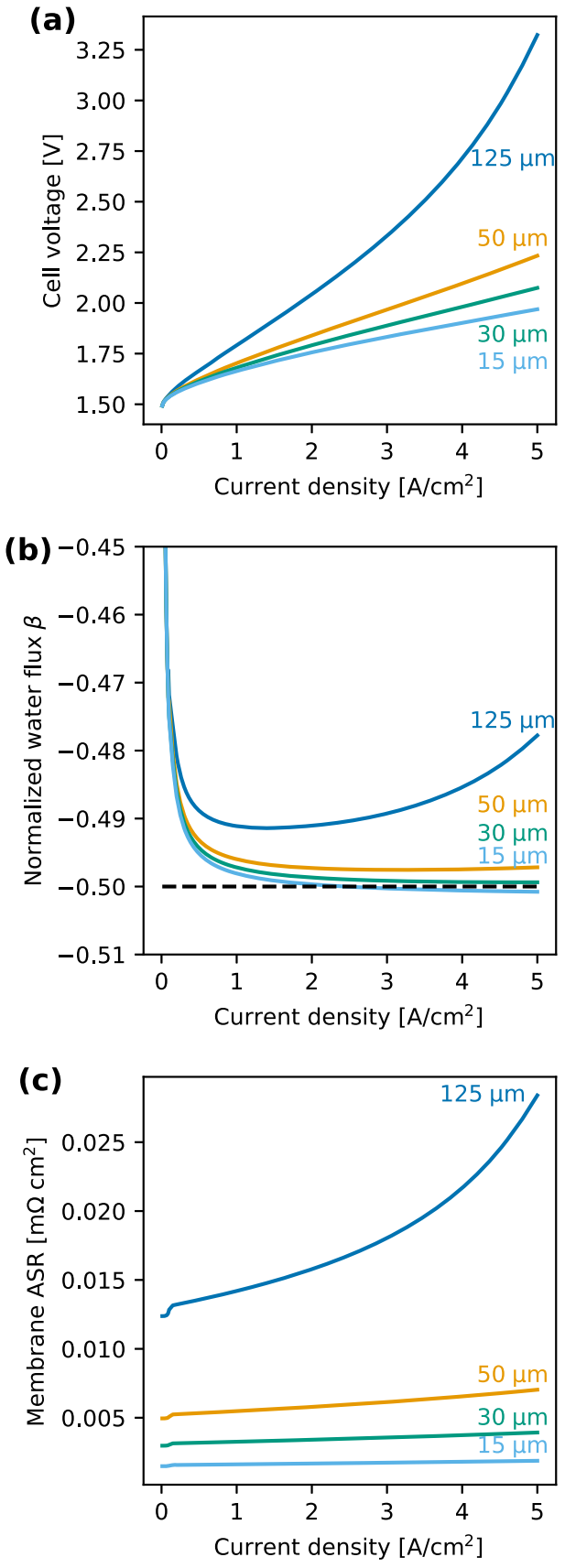

Figure 9. Simulated effect of varying the membrane thickness. **a.** Polarization curve, **b.** Normalized water flux and **c.** membrane ASR for each membrane thickness studied. The dashed line in **b** denotes the "break-even" point at which the water flux from cathode to anode exactly balances water consumption at the anode.

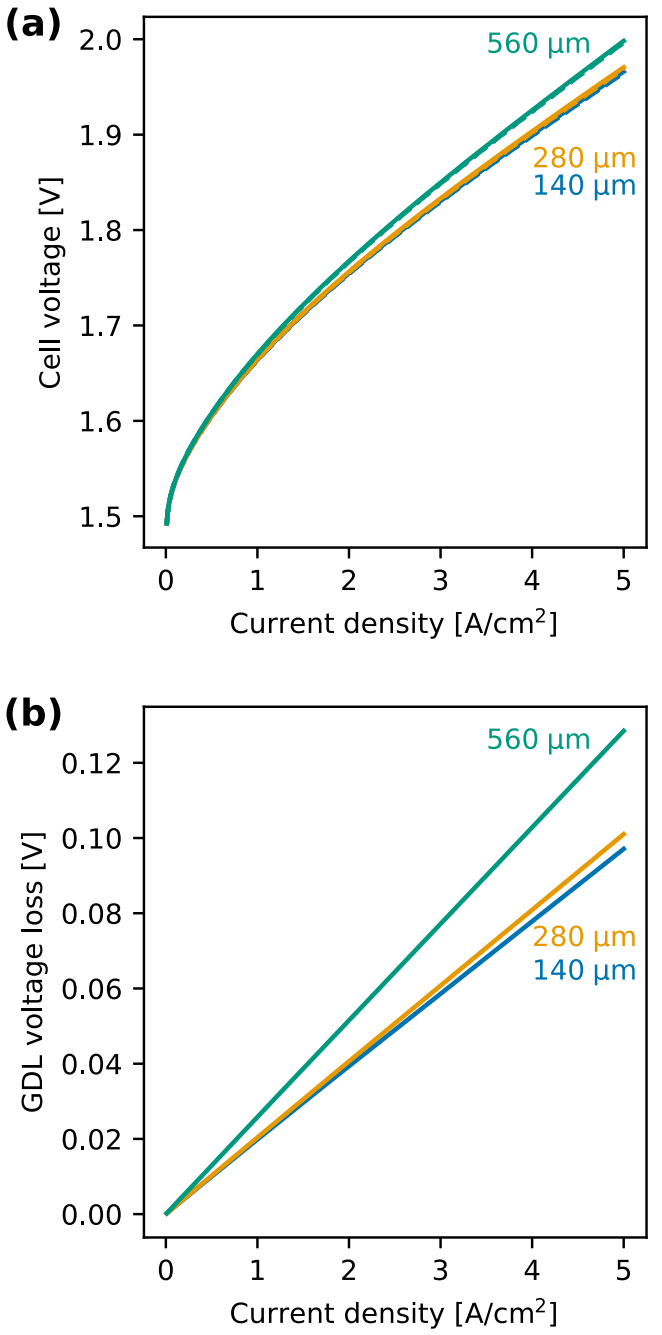

Figure 10. Simulated effect of varying the compressed thickness of the anode PTL and the cathode GDL. **a.** Polarization curves, **b.** voltage loss through the cathode GDL. Voltage loss was calculated as the difference between the average of ϕ_S at the GDL/CL interface and its average at the GDL/BPP interface.

Varying membrane thickness.—The thickness of the membrane plays a key role in keeping the anode well-hydrated. Membranes that are too thick will impede water transport from the cathode to the anode, resulting in anode dryout.

The effects of varying membrane thickness are shown in Fig. 9. Increasing the membrane thickness from 15 to 50 μm appears to only add resistive losses to the polarization curve, resulting in a uniform increase in slope as the membrane thickness is increased. Between 50 and 125 μm, however, the membrane becomes thick enough that water transport to the anode from the cathode is not fast enough to maintain high levels of membrane hydration. The membrane resistance thus increases with current density, which causes the polarization curve to bend upward at high current density.

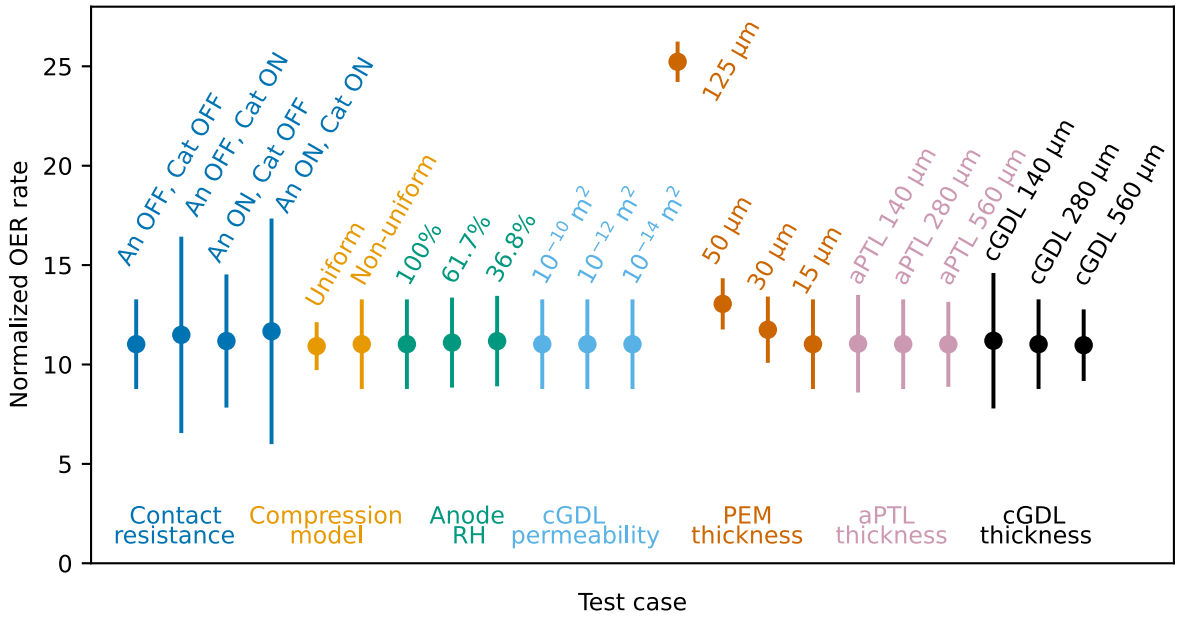

Figure 11. Mean normalized OER rate (points) and standard deviation (lines), calculated at the anode CL/membrane boundary, for each of the following test cases: varying contact resistance, compression effects, anode RH, cathode GDL permeability, membrane thickness, anode PTL compressed thickness with a cathode GDL thickness of 280 μm, and cathode GDL compressed thickness with an anode PTL thickness of 280 μm. The applied current is 4 A cm^{-2} in all cases. The OER rate is normalized by dividing the calculated rate by its expected value when uniformly distributed throughout the catalyst layer volume. A larger value of the mean normalized OER rate implies that the reaction rate is higher closer to the membrane.

In Fig. 9b, this phenomenon is visualized by normalizing the water flux to the current density:

$$\beta = \frac{N_{H_2O,M}}{N_{H^+}} = \frac{FN_{H_2O,M}}{i}, \qquad [29]$$

in which β represents the normalized water flux, $N_{H_2O,M}$ is the water flux through the membrane, F is Faraday's constant, and i is the current density. This normalization is also equivalent to normalizing by the proton flux N_{H^+}. In this case, a positive β value indicates that water is moving from the anode to the cathode, and a negative β value indicates water flux from cathode to anode. A β value of -0.5 indicates that enough water moves from the cathode to the anode to replace the water consumed at the anode stoichiometrically. Values of β above -0.5 indicate that water back-diffusion from the cathode to the anode does not completely compensate electroosmotic drag and water consumption, and the anode could begin to dry out. Values of β less than -0.5 indicate that water back-diffusion overcomes drag and consumption and the anode RH is expected to increase.

The normalized water flux plot (Fig. 9b) shows that, in most cases, water flux from cathode to anode is enough to balance water consumption at the anode, except for the 125 μm thick membrane. In that case, although cathode-to-anode water flux is enough to compensate over 95% of the water consumed at the anode, the remaining water consumption is enough to reduce membrane water content and thereby increase the area-specific resistance (Fig. 9c) as current density is increased.

Based on the results in Fig. 9, we recommend keeping the membrane thickness below 50 μm (that of Nafion^{TM} 212). Thicker membranes may be usable if the conductivity and water transport through them can be improved.

Influence of PTL and GDL thickness.—In addition to the permeabilities, the thicknesses of the cathode GDL and anode PTL can impact water transport while also affecting current distributions and local compression. Thicker and thinner cathode GDL and anode PTL thicknesses were studied with the model as shown in Fig. 10. The polarization curves cluster into two groups based on cathode GDL thickness. Increasing the cathode GDL thickness to 560 μm slightly increases cell voltage, whereas cell performance is insensitive to anode PTL thickness or decreasing cathode GDL thickness to 140 μm. The slight voltage increase on increasing cathode GDL thickness is due to increased resistive losses within the GDL as shown in Fig. 10b, which reports the difference between the average potential at the GDL/CL boundary and the average potential at the GDL/BPP boundary. Interestingly, the voltage losses do not decrease significantly if the GDL thickness is reduced below 280 μm. These diminishing returns of thinner PTLs are apparently due to a competition between decreased through-plane resistance and increased in-plane resistance. Since there is no electrical contact at the channel-GDL interface, electrical current must flow in-plane to reach the catalyst positioned between the channels. Although thinner GDLs exhibit less through-plane resistive losses due to the shorter conduction path, in-plane resistive losses increase, so the total GDL voltage losses do not scale linearly with GDL thickness.

Discussion

The OER reaction distribution is affected by CL contact resistances, compression uniformity, and the thicknesses of the GDL, PTL, and membrane materials. Figure 11 summarizes OER rate calculations from the model results discussed above by showing the mean value (filled circles) and standard deviation (vertical lines) of the OER rate along the anode CL/membrane boundary.

Thicker membranes result in water transport limitations, as shown above, and also cause the OER reaction distribution to shift closer to the anode CL/membrane boundary. As shown in Fig. 11, the mean OER rate along that boundary increases with thicker membranes. Water transport through the membrane to the anode is limiting performance in these thicker membranes, resulting in reduced ionomer conductivity within the anode CL. This reduction in conductivity shifts the OER reaction distribution closer to the membrane, raising the average OER rate at the membrane/CL interface.

Decreasing the CL contact resistances, increasing compression uniformity, or increasing the thicknesses of the GDL or PTL increases the uniformity of the OER rate along the anode CL/membrane boundary. This claim is supported by the reported standard deviation of the OER rate along the membrane/CL

boundary at the anode. The standard deviation of the OER rate increases when the cathode contact resistance is "switched on", and for the non-uniform compared to the uniform compression model. The standard deviation also increases with both decreasing anode PTL and cathode GDL thickness, though more significantly so in the cathode GDL study. These factors, namely the contact resistances, compression uniformity, and GDL/PTL thickness, all relate to electrical conductivity and contact between the catalyst layer and the GDL or PTL, further highlighting the importance of engineering this interface to maximize performance.

Conclusions

In this work, a two-dimensional steady-state physics-based model of a cathode liquid-fed proton-exchange-membrane water electrolyzer was developed, with particular care taken to understand compression-dependent conductivity and contact resistance properties in the GDL and CLs. Accounting for non-uniform compression could not explain the observed differences between soft and stiff cathode GDL materials, but including a compression-dependent contact resistance between the PTL and CL on the anode and the GDL and CL on the cathode explained much of the performance difference.

A key concern when feeding air to the anode is ensuring enough water transport to the anode CL to sustain OER. Sensitivity studies on GDL/PTL permeability, anode gas relative humidity, and membrane thickness were performed, highlighting membrane thickness and cross-membrane water transport as a key enabler for high-performing cathode liquid-fed PEM electrolyzers. If liquid water can get to the membrane through the cathode, the cell will have plenty of water to sustain OER at the anode given the thin membrane. If the membrane gets much thicker, however, water transport from the cathode to the anode will be more difficult, leading to dryout conditions at the anode. The model is fairly insensitive to changes in PTL and GDL thickness, indicating that a variety of porous media could be used as long as the conductivity and contact resistance properties are similar.

Non-uniform compression and contact resistance effects result in a non-uniform reaction distribution with a less-utilized portion of the electrolyzer catalyst above the channel. These non-uniformities can be reduced by reducing contact resistances, compressing the cell as uniformly as possible, and using thicker PTL or GDL materials.

Acknowledgments

This work has been performed within the MODELYS (Electrolyzer 2030—Cell and stack designs) and HYSTACK (Low cost, high efficiency PEM electrolyzer stack) projects financially supported by the Research Council of Norway under project numbers 326 809 and 321 466, respectively. We thank Dr. Luis Colmenares Rausseo for helpful discussions and Øyvind Lindgård, Firdaus Hendricks and Jannicke Kvello for data collection.

Appendix

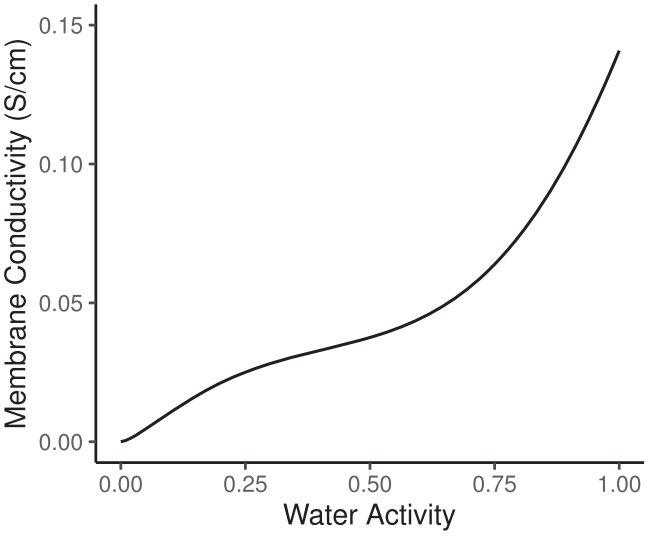

Figure A·1. Relationship between water activity and membrane conductivity used in the model.[17]

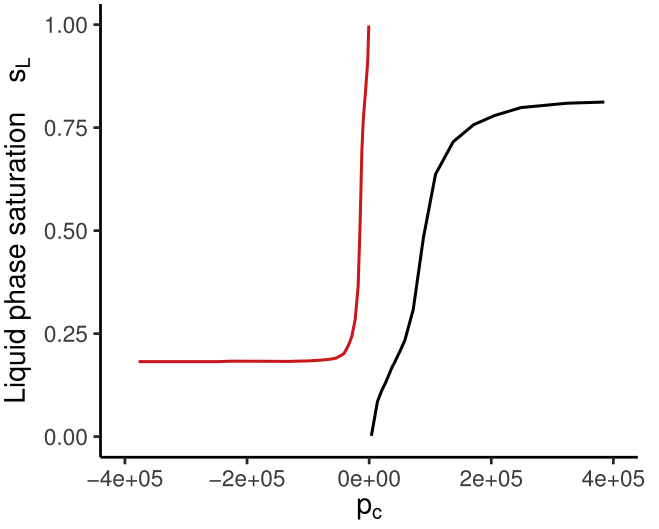

Figure A·2. Original mercury porosimetry data (black) and data corrected for hydrophilic air-water systems (red) using Eq. 16.

Table A·I. Membrane property data and relationships.

Symbol	Name	Definition
$c_{H_2O,M}$	Concentration of water in membrane	$\frac{\lambda}{\bar{V}_L\lambda + \bar{V}_M}$
$D_{H_2O,M}$	Water diffusivity in the membrane[20]	$(2.26 \times 10^{-5}\ \text{cm}^2\ \text{s}^{-1})\epsilon_{H_2O,M} \exp\left[\frac{E_{a,D}}{R}\left(\frac{1}{273.16\ \text{K}} - \frac{1}{T}\right)\right]$
$E_{a,D}$	Activation energy for diffusion[27]	$20000\ \text{J mol}^{-1}$
$E_{a,\kappa}$	Activation energy for proton conduction	$15000\ \text{J mol}^{-1}$
EW_M	Equivalent weight	$1100\ \text{g mol}^{-1}$
K_{sat}	Saturated permeability of membrane[17]	$1.8 \times 10^{-14}\ \text{cm}^2$
r_0	Characteristic membrane pore radius[17]	1.25 nm
r_c	Critical radius for water-filled membrane pores	$-2\gamma_{LG}\cos\theta(p_{L,M})^{-1}$
S	Fraction of liquid-equilibrated membrane[17]	$\frac{1}{2}\left[1 - \text{erf}\left(\frac{\ln r_c/r_0}{0.3\sqrt{2}}\right)\right]$
$\bar{V}_M$	Molar volume of membrane	$\frac{EW_M}{\rho_M} = 0.58\ \text{L mol}^{-1}$
$x_{H_2O,M}$	Mole fraction of water in membrane	$\frac{\lambda}{1+\lambda}$
α_{eff}	Effective water transport coefficient	$(1-S)\alpha_V + S\alpha_L$
α_L	Liquid-equilibrated water transport coefficient	$\frac{K_{sat}}{\eta_L \bar{V}_L^2}\left(\frac{\epsilon_{H_2O,M}}{\epsilon_{H_2O,M,max}}\right)^2 \epsilon_M^{1.5}$
α_V	Vapor-equilibrated water transport coefficient	$\frac{c_{H_2O} D_{H_2O} \epsilon_M^{1.5}}{RT(1-x_{H_2O,M})}$
$\epsilon_{H_2O,M}$	Volume fraction of water in membrane	$\frac{\lambda \bar{V}_L}{\bar{V}_M + \lambda \bar{V}_L}$
ϵ_M	Ionomer phase volume fraction	1 in the membrane, 0.5 in CLs
θ	Membrane-water contact angle[17]	90.02°
κ_{eff}	Effective ionic conductivity	$(1-S)\kappa_V + S\kappa_L$
κ_0	Conductivity prefactor	$0.5\ \text{S cm}^{-1}$
κ_L	Liquid-equilibrated proton conductivity (see Fig. A·1)	$\kappa_0(0.24)^{1.5}\ \epsilon_M^{1.5} \exp\left[\frac{E_{a,\kappa}}{R}\left(\frac{1}{303\ \text{K}} - \frac{1}{T}\right)\right]$
κ_V	Vapor-equilibrated proton conductivity (see Fig. A·1)	$\kappa_0(\epsilon_{H_2O,M} - 0.06)^{1.5}\ \epsilon_M^{1.5} \exp\left[\frac{E_{a,\kappa}}{R}\left(\frac{1}{303\ \text{K}} - \frac{1}{T}\right)\right]$
λ	Number of water molecules per charged group	$(1-S)\lambda_V + S\lambda_L$
λ_L	Number of water molecules per charged group, liquid-equilibrated	13.59
λ_V	Number of water molecules per charged group, vapor-equilibrated[28]	$35.12a_{H_2O,M}^3 - 43.49a_{H_2O,M}^2 + 21.96a_{H_2O,M}$
ξ	Electroosmotic coeffcient	1
ρ_M	Density of membrane	$1.9\ \text{g cm}^{-3}$

Table A·II. Thermodynamic relations for water in each phase modeled. The thermodynamic properties of water used in the model are listed in Table A·III.

Symbol	Name	Definition
$a_{H_2O,M}$	Activity of water in membrane	$\frac{p_{H_2O,sat}}{p_t}\exp[(\mu_{H_2O,M} - H_{H_2O,V}M_{H_2O}[1 - T/T_t] - C_{p,H_2O,V}M_{H_2O}[T - T_t - T\ln(T/T_t)])(RT)^{-1}]$
$p_{L,M}$	Liquid water pressure in membrane, Pa	$p_t + (\mu_{H_2O,M} + H_L M_L[1 - T/T_t] - C_{p,H_2O,L}M_L[T - T_t - T\ln(T/T_t)])\bar{V}_L^{-1}$
$\mu_{H_2O,V}$	Chemical potential of water, vapor, J/mol	$H_{H_2O,V}M_{H_2O}(1 - T/T_t) + RT\ln\left(\frac{p_{H_2O,V}}{p_t}\right) + C_{p,H_2O,V}M_{H_2O}[T - T_t - T\ln(T/T_t)]$
$\mu_{H_2O,L}$	Chemical potential of water, liquid, J/mol	$H_{H_2O,L}M_{H_2O}(1 - T/T_t) + \bar{V}_{H_2O,L}(p_L - p_t) + C_{p,H_2O,L}M_{H_2O}[T - T_t - T\ln(T/T_t)]$

Table A·III. Thermodynamic properties of water.

Symbol	Name	Definition
M_{H_2O}	Molar mass of water	18.016 g mol^{-1}
$\bar{V}_L$	Molar volume of liquid water	1.8×10^{-2} L mol^{-1}
γ_{LG}	Liquid-vapor surface tension of water	7.6×10^{-4} N cm^{-1}
$H_{H_2O,V}$	Enthalpy of water vapor	2500.8 J g^{-1}
$H_{H_2O,L}$	Enthalpy of liquid water	0 J g^{-1}
ΔH_{LV}	Enthalpy of vaporization of water	2500.8 J g^{-1}
p_t	Triple point pressure	611.2 Pa
T_t	Triple point temperature	273.16 K
$C_{p,H_2O,L}$	Heat capacity of liquid water	4.217 J g^{-1} K^{-1}
$C_{p,H_2O,V}$	Heat capacity of water vapor	1.854 J g^{-1} K^{-1}

Table A·IV. Liquid and gas properties relevant to the two-phase-flow model.

Symbol	Name	Definition
s_G	Gas saturation	$\max[(1 - s_L), 0.1]$
s_L	Liquid saturation	Computed from corrected data in Fig. A·2
ρ_G	Density of gas, kg m^{-3}	$\frac{p_G}{RT}\sum_i M_i x_i$
ρ_L	Density of liquid water[a]	983.3 kg m^{-3}
η_L	Viscosity of liquid water[a]	4.71×10^{-4} Pa s
η_G	Viscosity of gas[b]	$\sum_i \frac{x_i \eta_i}{x_i + \sum_j x_j \Phi_{ij}}$
Φ_{ij}	Viscosity correction factor[b]	$\frac{\sqrt{2}}{4}\left(1 + \frac{M_i}{M_j}\right)^{-0.5}\left(1 + \left(\frac{\eta_i}{\eta_j}\right)^{0.5}\left(\frac{M_j}{M_i}\right)^{0.25}\right)^2$
η_{H_2}	Hydrogen viscosity[b]	8.39×10^{-6} Pa s
η_{O_2}	Oxygen viscosity[b]	19.2×10^{-6} Pa s
$\eta_{H_2O,V}$	Water vapor viscosity[b]	8.02×10^{-6} Pa s
η_{N_2}	Nitrogen viscosity[b]	1.66×10^{-6} Pa s

a) Definition obtained from the COMSOL Material Library for liquid water at 333 K. b) Following the approach of Balliet et al.[29] using their values for component viscosities.

Table A·V. Binary diffusion coefficients for gaseous species, in Pa cm^2 s^{-1}. Coefficients are taken from correlations in Ref. 30 Chapter 17.

pD_{ij} (Pa cm^2 s^{-1})	N_2	H_2O
H_2	$4900\left(\frac{T}{64.83\ \mathrm{K}}\right)^{1.823}$	$24700\left(\frac{T}{146.82\ \mathrm{K}}\right)^{2.334}$
O_2	$5200\left(\frac{T}{139.59\ \mathrm{K}}\right)^{1.823}$	$29100\left(\frac{T}{316.14\ \mathrm{K}}\right)^{2.334}$
N_2	—	$24100\left(\frac{T}{285.81\ \mathrm{K}}\right)^{2.334}$

ORCID

Michael R. Gerhardt https://orcid.org/0000-0002-1272-3607
Jenny S. Østenstad https://orcid.org/0009-0008-4794-2552
Alejandro O. Barnett https://orcid.org/0000-0003-1328-7824
Magnus S. Thomassen https://orcid.org/0000-0002-8963-168X

References

1. K. Ayers, N. Danilovic, R. Ouimet, M. Carmo, B. Pivovar, and M. Bornstein, "Perspectives on low-temperature electrolysis and potential for renewable hydrogen at scale." *Annual Review of Chemical and Biomolecular Engineering*, **10**, 219 (2019).
2. M. S. Thomassen and A. O. Barnett, "A method for producing hydrogen in a PEM water electrolyser system, PEM water electrolyser cell, stack and system." *International Patent Application*, WO2019/009732 A2 (2019), https://patentscope.wipo.int/search/en/detail.jsf?docId=WO2019009732.
3. A. Z. Weber et al., "A critical review of modeling transport phenomena in polymer-electrolyte fuel cells." *J. Electrochem. Soc.*, **161**, F1254 (2014).
4. J. C. Fornaciari, M. R. Gerhardt, J. Zhou, Y. N. Regmi, N. Danilovic, A. T. Bell, and A. Z. Weber, "The role of water in vapor-fed proton-exchange-membrane electrolysis." *J. Electrochem. Soc.*, **167**, 104508 (2020).
5. J. S. Østenstad, "Multiphysical modeling of a next generation PEM electrolyser." *Master's Thesis*, Norwegian University of Science and Technology, Trondheim, Norway (2023).
6. T. Schuler, J. M. Ciccone, B. Krentscher, F. Marone, C. Peter, T. J. Schmidt, and F. N. Büchi, "Hierarchically structured porous transport layers for polymer electrolyte water electrolysis." *Adv. Energy Mater.*, **10**, 1903216 (2020).
7. E. Leonard, A. D. Shum, N. Danilovic, C. Capuano, K. E. Ayers, L. Pant, A. Z. Weber, X. Xiao, D. Y. Parkinson, and I. V. Zenyuk, "Interfacial analysis of a PEM electrolyzer using X-ray computed tomography." *Sustainable Energy & Fuels*, **4**, 921 (2020).
8. A. C. Olesen, C. Rømer, and S. K. Kr, "A numerical study of the gas-liquid, two-phase flow maldistribution in the anode of a high pressure PEM water electrolysis cell." *International Journal of Hydrogen Energy*, **41**, 52 (2016).
9. A. C. Olesen, S. H. Frensch, and S. K. Kr, "Towards uniformly distributed heat, mass and charge: A flow field design study for high pressure and high current density operation of PEM electrolysis cells." *Electrochimica Acta*, **293**, 476 (2019).
10. J. Kleemann, F. Finsterwalder, and W. Tillmetz, "Characterisation of mechanical behaviour and coupled electrical properties of polymer electrolyte membrane fuel cell gas diffusion layers." *Journal of Power Sources*, **190**, 92 (2009).
11. I. Nitta, T. Hottinen, O. Himanen, and M. Mikkola, "Inhomogeneous compression of PEMFC gas diffusion layer Part I. Experimental." *Journal of Power Sources*, **171** (1), 26 (2007).
12. I. Nitta, O. Himanen, and M. Mikkola, "Contact resistance between gas diffusion layer and catalyst layer of PEM fuel cell." *Electrochemistry Communications*, **10**, 47 (2008).
13. T. G. Tranter, J. T. Gostick, A. D. Burns, and W. F. Gale, "Pore network modeling of compressed fuel cell components with OpenPNM." *Fuel Cells*, **16**, 504 (2016).
14. D. Ješić, D. Lašič Jurković, A. Pohar, L. Suhadolnik, and B. Likozar, "Engineering photocatalytic and photoelectrocatalytic CO2 reduction reactions: Mechanisms, intrinsic kinetics, mass transfer resistances, reactors and multi-scale modelling simulations." *Chemical Engineering Journal*, **407**, 126799 (2021).

15. D. S. Falcão and A. M. F. R. Pinto, "A review on PEM electrolyzer modelling: Guidelines for beginners." *Journal of Cleaner Production*, **261**, 121184 (2020).
16. M. R. Gerhardt, L. M. Pant, J. C. Bui, A. R. Crothers, V. M. Ehlinger, J. C. Fornaciari, J. Liu, and A. Z. Weber, "Methodpractices and pitfalls in voltage breakdown analysis of electrochemical energy-conversion systems." *J. Electrochem. Soc.*, **168**, 074503 (2021).
17. A. Z. Weber and J. Newman, "Transport in Polymer-Electrolyte Membranes : II. Mathematical Model." *J. Electrochem. Soc.*, **151**, A311 (2004).
18. N. Li, S. S. Araya, X. Cui, and S. K. Kr, "The effects of cationic impurities on the performance of proton exchange membrane water electrolyzer." *Journal of Power Sources*, **473**, 228617 (2020).
19. M. Prestat, "Corrosion of structural components of proton exchange membrane water electrolyzer anodes: A review." *Journal of Power Sources*, **556**, 232469 (2023).
20. I. V. Zenyuk, P. K. Das, and A. Z. Weber, "Understanding impacts of catalyst-layer thickness on fuel-cell performance via mathematical modeling." *J. Electrochem. Soc.*, **163**, F691 (2016).
21. G. Serre, M. Chandesris, F. Fouda-Onana, D. Brun-Buisson, P. Skjetne, T. Bergstrøm, K. Bromberger, T. Smolinka, and J. Ghinaiya, *MEGASTACK: D2.3 Functional and validated multi-scale and multi-phase models for PEM water electrolyzer RT/DEHT/2016-137*, Commissariat à l'énergie atomique et aux énergies alternatives (2016), https://sintef.no/contentassets/f8060684df6f459da532c-b3aec6b8c02/megastack-d2.3.pdf.
22. M. R. Gerhardt, L. M. Pant, and A. Z. Weber, "Along-the-channel impacts of water management and carbon-dioxide contamination in hydroxide-exchange-membrane fuel cells: a modeling study." *J. Electrochem. Soc.*, **166**, F3180 (2019).
23. S. A. Grigor'ev, M. M. Khaliullin, N. V. Kuleshov, and V. N. Fateev, "Electrolysis of water in a system with a solid polymer electrolyte at elevated pressure." *Russian Journal of Electrochemistry*, **37**, 819 (2001).
24. K. C. Neyerlin, W. Gu, J. Jorne, and H. A. Gasteiger, "Study of the exchange current density for the hydrogen oxidation and evolution reactions." *J. Electrochem. Soc.*, **154**, B631 (2007).
25. H. Wang, M. A. Sweikart, and J. A. Turner, "Stainless steel as bipolar plate material for polymer electrolyte membrane fuel cells." *Journal of Power Sources*, **115**, 243 (2003).
26. European Commission, Joint Research Centre, G. Tsotridis, A. Pilenga, and T. Malkow et al., *EU harmonised polarisation curve test method for low-temperature water electrolysis*, Publications Office (2018).
27. M. Carmo, D. L. Fritz, J. Mergel, and D. Stolten, "A comprehensive review on PEM water electrolysis." *International Journal of Hydrogen Energy*, **38**, 4901 (2013).
28. K. G. Gallagher, B. S. Pivovar, and T. F. Fuller, "Electro-osmosis and Water Uptake in Polymer Electrolytes in Equilibrium with Water Vapor at Low Temperatures." *J. Electrochem. Soc.*, **156**, B330 (2009).
29. R. J. Balliet and J. Newman, "Cold start of a polymer-electrolyte fuel cell I. Development of a two-dimensional model." *J. Electrochem. Soc.*, **158**, B927 (2011).
30. R. B. Bird, W. E. Stewart, and E. N. Lightfoot, *Transport Phenomena* (John Wiley & Sons, New York, NY) 2nd ed. (2002).